International Journal of Refractory Metals and Hard Materials 111 (2023) 106053

Contents lists available at ScienceDirect

International Journal of Refractory Metals and Hard Materials

journal homepage: www.elsevier.com/locate/IJRMHM

A computational framework for micromechanical modelling of WC-Co composites

Pedro Vinícius Sousa Machado [a], Ferhun C. Caner [a,*], Luis Llanes [a,b], Emilio Jimenez Pique [a,b]

[a] Department of Materials Science and Engineering, EEBE – Campus Diagonal Besòs, Universitat Politècnica de Catalunya – BarcelonaTech, 08019 Barcelona, Spain
[b] Barcelona Research Center in Multiscale Science and Engineering, Campus Diagonal Besòs, Universitat Politècnica de Catalunya – BarcelonaTech, 08019 Barcelona, Spain

ARTICLE INFO

Keywords:
Ceramic-metal composites
Finite element analysis
Micromechanical modelling
WC-co cemented carbides

ABSTRACT

In this study, the mechanical behavior under monotonic loads of tungsten carbide-cobalt (WC-Co) composites is investigated extensively by analyzing (1) nanoindentation tests on WC particles and Co matrix, (2) nanowires made of WC-Co composites tested in tension and (3) micropillars made of WC-Co composites tested in compression. To this end, a novel computational framework consisting of two different microplane constitutive models developed for WC and Co phases are proposed. For the Co matrix, the microplane J_2-plasticity, called the model MPJ2, and for the WC particles a modified version of the microplane model M7, called the model M7WC, are employed. Furthermore, finite element meshes in 3D obtained from experimental tomography reconstructions of WC-Co composites are employed to rule out any spurious geometric features that is likely to be encountered in artificially generated meshes. After calibrating the aforementioned models, it is shown that the finite element predictions not only confirm the extensive experimental observations but also shed further light into the mechanical behavior of these composites.

1. Introduction

WC-Co cemented carbides, often simply termed hardmetals, are forefront materials in many tooling and engineering applications, such as metal cutting, mining, rock drilling, metal forming, structural components, and wear parts [1] because of their outstanding properties such as high hardness, high strength and high wear resistance. These outstanding properties result not only from their composite nature, meaning they combine constitutive phases with quite different attributes but also the optimal interface properties of the WC-Co system [2]. Depending on the metallic phase content, the state of aggregation of the ceramic hard phase may range from quasi-isolated ceramic particles dispersed in the binder phase (high metal content) to a highly connected skeleton of contiguous carbide grains for grades with low binder content [3]. Hence, considering that compositions of commercial grades range from 3 to 30_{wt}% of metallic binder, cemented carbides may be micromechanically described as composites of ceramic nature (rather than metal-based) reinforced by ductile metallic ligaments, strengthened through the constraint imposed by the very rigid carbide crystals [4–9].

Small-scale mechanical tests such as nanoindentation [10,11], uniaxial tensile tests of nanowires [12] and micropillar compression [13,14], permit the assessment of the mechanical behavior of small volumes of material as well as single phases. These are relevant to study not only the contact and wear behaviors but also the behavior under monotonic loads, where the overall performance of a tool is dictated by the behavior of the material at small length scales. Furthermore, such tests allow in-situ visualization and post-mortem inspection of the complete microstructure, key to capture the inherent deformation mechanisms. Although results from these tests may have several types of uncertainties [15–18], they still provide one of the best characterization strategies to closely analyze the local inelastic behavior at micro- and nanometric dimensions.

Most studies on simulation of the mechanical behavior of WC-Co cemented carbides consider the microstructure of these composites either in 2D or in the so called 2.5D [19–23]. Those in 3D use computationally generated microstructures [24,25] that may fail to capture entirely the true nature of the material. A better approach is constructing 3D meshes based on real sequential sectioning of the microstructure, using, for instance, focused ion beam (FIB) tomography [26]. In this case, achieved resolution is high enough to capture the interconnecting WC grains and binder skeletons.

Moreover, WC carbides have been mostly modelled as either

* Corresponding author.
E-mail address: ferhun.caner@upc.edu (F.C. Caner).

https://doi.org/10.1016/j.ijrmhm.2022.106053
Received 5 September 2022; Received in revised form 21 October 2022; Accepted 23 November 2022
Available online 28 November 2022

isotropic elastic [20–33] or anisotropic elastic [34,35]. For damage, critical stress criteria [30,31] and fracture energy criteria [34] have been used. The WC carbides, however, are brittle under tension but can sustain moderate plastic strain when under compression [12–14]. This is an important behavior that these previous studies were not able to capture. On the other hand, the Co binder has been modelled as elastoplastic with strain hardening [20,24,28,32,33,34,36], and viscoelasticity [21,22,35]. For damage, plastic strain accumulation criteria have been used [21,34].

In this study, we aim to create a computational framework for the mechanical behavior of WC-Co composites by using the microplane modelling approach [37–40], together with a realistic mesh based on FIB tomography images [26]. Contrary to other models, with the microplane approach it is easy to distinguish the mechanical behavior under different loading conditions. At the same time, these realistic meshes are more representative of the true composite nature of the material microstructure and have no spurious geometric features that are likely to exist and cause problems in computationally generated meshes. The proposed computational approach is first calibrated by fitting micropillar compression test data from fine-grained composite (FGC), three-point bending test data from FGC beams and uniaxial tension test data from a pure Co specimen. Next, it is validated by comparing model prediction outcomes with experimentally attained nanoindentation data on WC and Co particles [10,11]; uniaxial tensile test data on coarse-grained composite (CGC) nanowires [12]; and CGC and FGC micropillar compression test data [13,14].

2. Finite element analyses

Two distinct phase assemblages of WC-Co composites are considered in this study: A fine-grained composite with 10.5% wt. Co (FGC) and a coarse-grained one with 22.4% wt. Co (CGC). The finite element meshes generated for the simulations of nanoindentation, nanowire tension and micropillar compression are shown in Fig. 1, Fig. 3 and Fig. 11 respectively. In this work, the analysis of micropillar compression receives more attention, partly because the availability of a wider range of experimental data.

Another novelty in the computational framework presented are the constitutive models used for WC particles and Co binder. For the constitutive model for the metallic binder, the microplane J_2-plasticity (MPJ2) model is used [37]. The advantage of implementing this model, instead of the classical J_2-plasticity, is that the former allows selective activation of the slip planes, based on the resolved shear stress on these planes using a yield surface unique to each of these planes. Thus, model MPJ2 involves many yield surfaces, opposite to the classical J_2-plasticity which typically employs only one yield surface. Consequently, the transition from elastic regime to the elastoplastic one takes place more smoothly when the model MPJ2 is used. The constitutive model for the WC carbide is chosen to be a modified version of the microplane model M7 [38–40], here referred to as M7WC. Model M7 was originally developed for multiaxial inelastic damage and fracture behavior of concrete; thus, it is an ideal one for simulating the mechanical behavior of any ceramic based quasi-brittle material, as it would be the case of ceramic-base composites. M7 uses the so-called stress-strain boundaries (or strain-dependent yield surfaces) on every potential plane of inelastic deformation to model the complex multiaxial mechanical behavior of such materials. In the last decade, M7 has been extended to model fiber-reinforcement [41], fatigue behavior [42], alkali-silica reaction effects [43], and high strain-rate behavior [44] of concrete. However, to apply the model M7 to WC particles, it turns that it must be modified significantly which gives rise to the model M7WC applicable to the WC particles.

One of the key points of this study is the finite element meshes generated by sequential FIB (S-FIB) tomography, allowing the use of real microstructural geometry for both micropillars and nanowires. A mesh based on real microstructure images is more realistic than those which are computer-generated, thus facilitating substantially the modelling of the material behavior. In the case of the nanoindentation simulations, because the deformations are localized within either the WC particle or the Co phase, meshes are simply generated using Abaqus, i.e. real microstructural features of the material are not considered to reduce the computational cost of the simulations.

Aiming to get micropillar and nanowire meshes, S-FIB images reported in [26] are imported to the commercial software Avizo. Then, a tetrahedral mesh is created after trimming, as shown in Fig. 1. Subsequently, each tetrahedron is converted into four hexahedra. The final mesh has approximately 2500 and 130,000 bilinear hexahedral elements in nanowire and micropillar simulations respectively. Examples of a meshed micropillar specimen in compression as well as a meshed nanowire specimen in tension are shown in Fig. 2 (a) and Fig. 2 (b) respectively. In Table 1, average values of microstructural features for micropillars [13,14] and nanowires [12] are listed, as reported in the original experimental studies. In the case of nanowires, representative microstructural information is difficult to define, as given information is limited to average WC particle size and WC-to-Co ratio (and even phase contiguity) was different for all tested specimens [12]. Considering the former is rather coarse and the latter ranged from values of cobalt area fraction between 10 and 40%, nanowire meshes in this study were produced using the S-FIB tomography data for CGC grade.

Dimensions of the simulated micropillars and nanowires, together with those of specimens used in the experiments, are compared in Table 2. It may be observed that the analyzed micropillars and

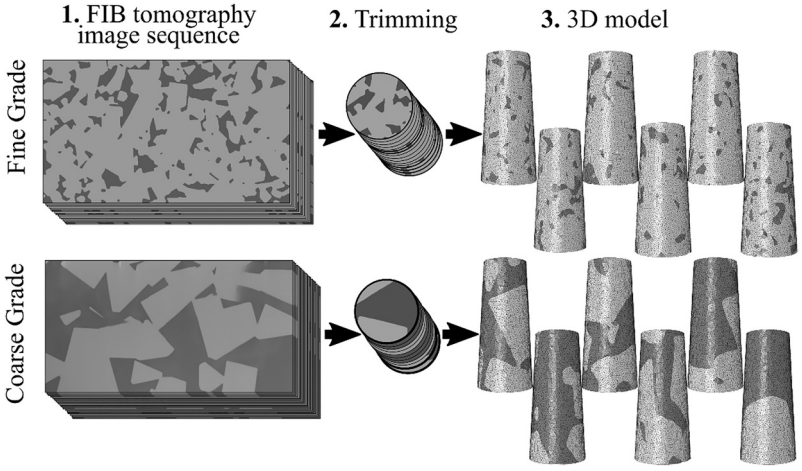

Fig. 1. Generation of the 3D micropillar models.

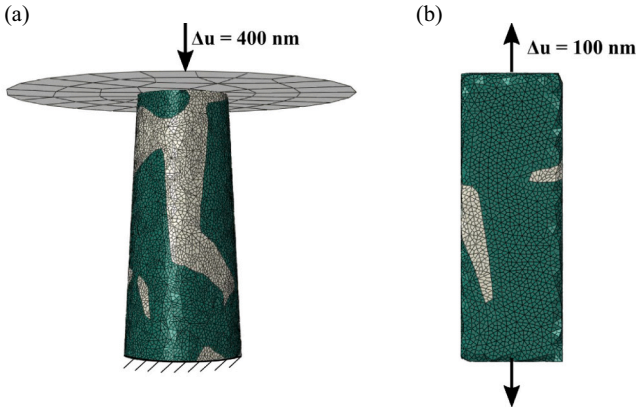

Fig. 2. (a) Simulation conditions of micropillars in compression; (b) nanowires in tension.

Table 1
Microstructure parameters of the meshes used in the simulations [26], compared with micropillars tested in studies [14] and [13] and nanowires tested in [12].

	CGC [26]	FGC [26]	FGC [14]	CGC [13]	CGC [12]
Binder Volume (%)	35.0	17.5	–	–	10–40
Binder Weight (%)	22.4	10.5	10	15	
Mean WC Size (μm)	1.6	0.4	0.4	–	2.0
Contiguity	0.30	0.56	0.20	–	–
Mean Free Path (μm)	1.26	0.19	0.50	–	–

nanowires are very similar to the samples tested in the experimental works, in terms of both geometry and relative amount of constitutive phases.

The meshes used for the nanoindentation simulations of WC and Co are shown in Fig. 3 (a) and (b), respectively. They consist of 712,448 and 2,000,376 bilinear hexahedral elements, respectively, and are generated using Abaqus. In Fig. 3 (c), the rigid Berkovich indenter is shown penetrating the samples. The samples are represented by hemispheres of 36 μm and 72 μm in diameter for the WC and Co phases, with corresponding penetration depths of 900 nm and 1900 nm respectively. It is noted that the hemispheres simulating the specimens must be much larger in diameter than the maximum penetration depth (about 36 times larger in this study) not only to minimize the influence of the boundary conditions on the results but also to keep the computational cost from rising too high.

2.1. M7WC model

Attempting to describe the constitutive behavior of the ceramic phase, i.e. WC particles, the model M7WC, a modified version of the model M7, is employed. In model M7 [38,39], the strain tensor $\boldsymbol{\varepsilon}$ with components ϵ_{ij} (where $i, j = 1$ *to* 3) is projected onto "microplanes" at a given material point, as shown in Fig. 4. The strain vector on any given microplane is to be input to a constitutive relation which yields stress on the same microplane. This is called the kinematic constraint. Thus, the model M7 is a kinematically constrained microplane model. Kinematic constraint is necessary for capturing strain-softening behavior of quasi-brittle materials like WC.

In order to represent each microplane, its corresponding unit normal vector $\hat{\boldsymbol{n}}$ and shear vectors $\hat{\boldsymbol{m}}$ and $\hat{\boldsymbol{l}}$ are used. Aiming to avoid any

Table 2
Dimensions of small-scale specimens used in [14], [13] and [12], as compared to those of the simulated micropillars and nanowires.

	Simulated CGC and FGC micropillars	CGC micropillars in [13]	FGC micropillars in [14]	Simulated CGC nanowires	CGC nanowires in [12]
Aspect ratio (l/d_{top})	2.9	2 to 2.5	3.3	–	–
Taper angle (degrees)	3	2 to 3	3.4	–	–
Top Diameter (μm)	2.1	2.5 to 3	2.1	–	–
Thickness (μm)	–	–	–	0.4	0.2 to 0.5
Width (μm)	–	–	–	1.4	0.3 to 1.5
Length(μm)	–	–	–	4	3.7 to 4.7

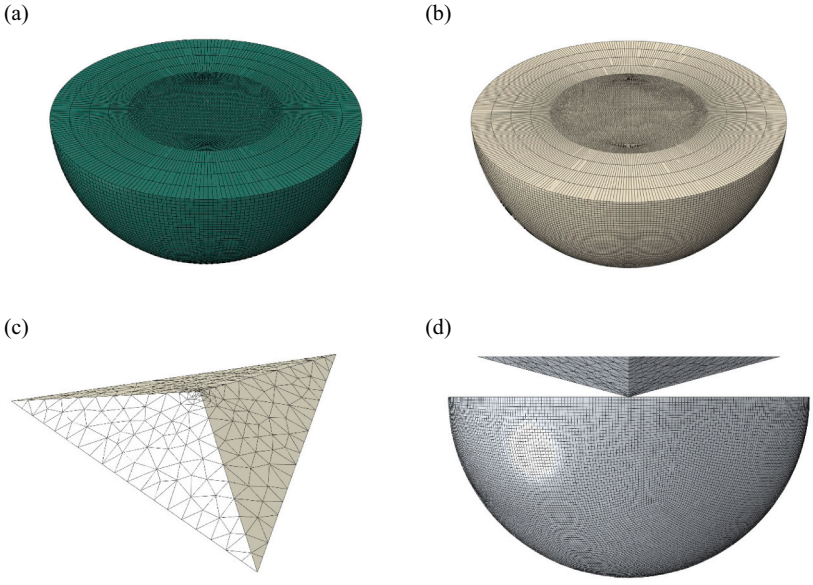

Fig. 3. (a) WC, (b) Co hemispheres to be indented by the (c) Berkovich indenter; (d) model assembly.

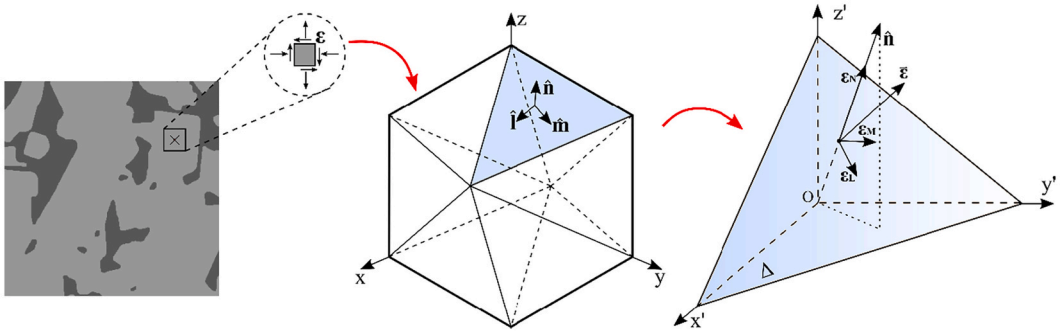

Fig. 4. Microplane system with kinematic constraint.

directional bias, $\hat{\boldsymbol{m}}$ is given a random direction; and then, $\hat{\boldsymbol{l}}$ is defined as $\hat{\boldsymbol{l}} = \hat{\boldsymbol{n}} \times \hat{\boldsymbol{m}}$. Hence, the 3 microplane strain components at each microplane are calculated as $\varepsilon_N = N_{ij}\epsilon_{ij}$, $\varepsilon_M = M_{ij}\epsilon_{ij}$ and $\varepsilon_L = L_{ij}\epsilon_{ij}$, where subscripts range from 1 to 3, $N_{ij} = n_i n_j$, $M_{ij} = (n_i m_j + n_j m_i)/2$ and $L_{ij} = (n_i l_j + n_j l_i)/2$. The microplane stress components σ_N, σ_M and σ_L are obtained using the corresponding constitutive relations as $\sigma_N = F_N(\varepsilon_N)$, $\sigma_T^2 = \sigma_L^2 + \sigma_M^2 = F_\tau\left(\sqrt{\epsilon_L^2 + \epsilon_M^2}\right)$ in tension ($\sigma_N > 0$). The stress tensor is calculated by considering the principle of virtual work:

$$\frac{2\pi}{3}\boldsymbol{\sigma} : \delta\boldsymbol{\varepsilon} = \int_\Omega (\sigma_N \delta\varepsilon_N + \sigma_M \delta\varepsilon_M + \sigma_L \delta\varepsilon_L) d\Omega \tag{1}$$

which leads to

$$\sigma_{ij} = \frac{3}{2}\pi \int_\Omega \left(\sigma_N N_{ij} + \sigma_L L_{ij} + \sigma_M M_{ij}\right) d\Omega \tag{2}$$

in tension ($\sigma_N > 0$). In compression ($\sigma_N < 0$), the macro-micro stress equilibrium equation becomes:

$$\sigma_{ij} = \frac{3}{2}\pi \int_\Omega \left(\sigma_D N_{ij} + \sigma_L L_{ij} + \sigma_M M_{ij}\right) d\Omega + \sigma_v \delta_{ij} \tag{3}$$

in which $\sigma_D = F_D(\epsilon_D)$ and $\sigma_V = F_V(\epsilon_V)$ are the deviatoric and volumetric parts of the microplane normal stress obtained from the corresponding constitutive functions.

Such an approach has some key advantages: (i) damage and cracking in the strain-softening regime [45] may be modelled; (ii) the constitutive equations are more intuitive on the microplane using vectors, instead of invariants of second order tensors; (iii) the vertex effect is automatically captured [46]; and (iv) boundary slip observed between WC particles can be captured. Its full algorithm is explained in [38], and the interested reader is referred to [29] for detailed information. However, there are two important modifications that have been made in the model M7, such that it may be satisfactorily applied to simulation of WC particle behavior. The first one refers to the volumetric boundary defined by Eqs.13 and 14 in [38], which has been modified as

$$\sigma_V^b = Ek_1k_3 exp(-\epsilon_V/k_1k_4) \tag{4}$$

The second one involves the shear boundary given by Eqs. 27 and 28 in [38], which has been replaced by

$$\sigma_\tau^b = \frac{k_1 k_2}{\left(1 + \frac{max(\varepsilon_\tau - c_{10}, 0)}{c_{11}}\right)^2} \tag{5}$$

where $\varepsilon_\tau = \sqrt{\varepsilon_L^2 + \varepsilon_M^2}$. These two relatively slight changes improve the model behavior drastically, particularly for the case of nanoindentation tests, as can be seen in Fig. 10. This modified model M7 is referred to in this work as M7WC.

2.2. MPJ2 model

Description of the constitutive behavior of the metallic phase, i.e. the Co binder, is achieved employing the MPJ2 model. It is based on a series of models first presented in Ref. [37], but that study lacked not only a detailed computational algorithm but also sufficiently extensive verification of the model. In this study, an in-depth computational algorithm in the finite strain range is presented. Moreover, in the results section it is shown that this model can predict nanoindentation, nanowires under tension, and micropillars under compression experiments.

In the classical J_2 plasticity the yield surface is expressed in terms of the second invariant of the deviatoric stress tensor

$$J_2 = \frac{1}{6}\left[(\sigma_I - \sigma_{II})^2 + (\sigma_{II} - \sigma_{III})^2 + (\sigma_{III} - \sigma_I)^2\right] \tag{6}$$

where σ_I, σ_{II} and σ_{III} are the principal values of $\boldsymbol{\sigma}$. The yield surface is set to expand as a function of the accumulated plastic strain, ϵ_p^{eff}:

$$J_2 = \tau^2\left(\epsilon_p^{eff}\right) \tag{7}$$

When elastic limit is reached, radial return of the stress state to the yield surface is then imposed. Isotropic-hardening is inappropriate for capturing the Bauschinger effect, which is generally remediated by the kinematic-hardening [47]. However, in the model MPJ2 the Bauschinger effect is obtained as a consequence of the loading and unloading interactions between different microplanes without using kinematic hardening.

In the model MPJ2, hardening is assumed to occur on a microplane when the inequality given by

$$\sigma_D^2 + \sigma_L^2 + \sigma_M^2 > \tau^2\left(\epsilon_p^{eff}\right) \tag{8}$$

is satisfied. In this equation, $\sigma_D = \sigma_N - \sigma_V$ is the microplane deviatoric stress, σ_M and $\sigma_L$are microplane shear stresses, $\sigma_N = N_{ij}\sigma_{ij}$ is the microplane normal stress, $\sigma_V = \sigma_{ii}/3$ (repeated indices imply summation) is the volumetric stress, and $\tau(\epsilon_p^{eff})$ is the hardening function defined on a microplane. The complete microplane J_2-plasticity model algorithm is as follows:

(i) The Green's Lagrangian strain tensor, appropriate for finite strain, is calculated using:

$$\boldsymbol{\varepsilon} = \frac{1}{2}\left(\boldsymbol{F}^T\boldsymbol{F} - \boldsymbol{I}\right) \tag{9}$$

where $\boldsymbol{F}$ is the deformation gradient tensor.

(ii) Cauchy-Green deformation tensor is computed using:

$$\boldsymbol{C} = 2 \bullet \boldsymbol{\varepsilon} + \boldsymbol{I} \tag{10}$$

(iii) Eigen values and eigen vectors of $\boldsymbol{C}$ are computed by using the Jacobi eigen value algorithm [48].

(iv) Considering the matrix $\boldsymbol{V} = [\boldsymbol{v_1}\ \boldsymbol{v_2}\ \boldsymbol{v_3}]$, where $\boldsymbol{v_1}$, $\boldsymbol{v_2}$ and $\boldsymbol{v_3}$ are the eigenvectors of $\boldsymbol{C}$, and the diagonal matrix $\boldsymbol{\Lambda}$ with components $\log(\lambda_1)$, $\log(\lambda_2)$ and $\log(\lambda_3)$, where λ_1, λ_2 and λ_3 are the eigenvalues of $\boldsymbol{C}$; the logarithmic strain $\boldsymbol{H}$ is computed using:

$$\boldsymbol{H} = \frac{1}{2}\boldsymbol{V}\boldsymbol{\Lambda}\boldsymbol{V}^T \tag{11}$$

(v) The logarithmic strain increment is calculated using:

$$\delta\boldsymbol{H} = \boldsymbol{H} - \boldsymbol{H}_{old} \tag{12}$$

(vi) The volumetric strain and its increment (ε_V and $\delta\varepsilon_V$) are determined as:

$$\varepsilon_V = lnJ/3 \tag{13}$$

$$\delta\varepsilon_V = (lnJ - lnJ_{old})/3 \tag{14}$$

where J is the determinant of $\boldsymbol{F}$.

Microplane and strain vectors (ε_N, ε_L and ε_M) and strain increments ($\delta\varepsilon_N$, $\delta\varepsilon_L$, $\delta\varepsilon_M$) are calculated with the logarithmic strain tensor $\boldsymbol{H}$ and its increment $\delta\boldsymbol{H}$, as: $\varepsilon_N = N_{ij}H_{ij}$, $\varepsilon_M = M_{ij}H_{ij}$ and $\varepsilon_L = L_{ij}H_{ij}$, and $\delta\varepsilon_N = N_{ij}\delta H_{ij}$, $\delta\varepsilon_M = M_{ij}\delta H_{ij}$ and $\delta\varepsilon_L = L_{ij}\delta H_{ij}$, where subscripts range from 1 to 3, $N_{ij} = n_i n_j$, $M_{ij} = (n_i m_j + n_j m_i)/2$ and $L_{ij} = (n_i l_j + n_j l_i)/2$.

(vii) The volumetric stress and its increment, which are the same for all microplanes, are computed as:

$$\delta\sigma_V = E_V\delta\varepsilon_V \tag{15}$$

$$\sigma_V = \sigma_{V\,old} + \delta\sigma_V \tag{16}$$

In Eq. (15), the elastic volumetric stiffness is defined as $E_V = E/(1 + 2\nu)$.

The deviatoric strain increment is then evaluated in each microplane as $\delta\varepsilon_D = \delta\varepsilon_N - \delta\varepsilon_V$.

(viii) The stress increments are computed as:

$$\sigma_K = \sigma_K^{old} + \delta\varepsilon_K E_T \tag{17}$$

where $K = D$, M or L and $E_T = E/(1 + \nu)$.

If the inequality

$$\sigma_D^2 + \sigma_M^2 + \sigma_L^2 \leq \tau^2(\varepsilon_{P\,old}) \tag{18}$$

is true at a given microplane, then the yield surface has not been exceeded; thus, the material is still in elastic regime, and no hardening takes place.

If the inequality (18) is false at a given microplane, then it means elastoplastic deformation occurs, and material hardens according to the normality rule. The values of σ_D, σ_M, σ_L radially return to the yield surface, and thus they are calculated as:

$$\sigma_K = \sigma_K - \frac{E_T\delta\epsilon_p^{old}\sigma_K^{old}}{\sqrt{\sigma_D^2 + \sigma_M^2 + \sigma_L^2}} \tag{19}$$

where $K = D$, L *or* M.

(ix) As a consequence of work hardening, the hardening function τ is now updated as:

$$\tau^2 = \left[\sqrt{3k_3\left(1 + \frac{\varepsilon_P}{k_2}\right)^{k_1}}\right]^2 \tag{20}$$

$$\varepsilon_P = \varepsilon_{P\,old} + \delta\varepsilon_P \tag{21}$$

$$\delta\varepsilon_P = max\left(\frac{\Delta\lambda_1}{\Delta\lambda_2}, 0\right) \tag{22}$$

where

$$\Delta\lambda_1 = \frac{E_T(\sigma_{D\,old}\delta\varepsilon_D + \sigma_{L\,old}\delta\varepsilon_L + \sigma_{M\,old}\delta\varepsilon_M)}{\sqrt{(\sigma_D^2 old + \sigma_M^2 old + \sigma_L^2 old)}} \tag{23}$$

$$\Delta\lambda_2 = E_T + \frac{\tau(\varepsilon_{P\,old})k_1}{k_2 + \varepsilon_{P\,old}} \tag{24}$$

(x) $\sigma_N = \sigma_V + \sigma_D$, on each microplane is computed.

(xi) Finally, the principle of virtual work given in Eq. (1) is applied to calculate the Cauchy stress tensor components.

3. Calibration

3.1. The model M7WC

The model M7WC is used to simulate the mechanical behavior of WC particles. Elastic modulus and Poisson's ratio are obtained from experiments from [20], but were further optimized to match the experimental values used in this section for calibration. The element size in the mesh is fixed at approximately 95 nm. However, this model has many more parameters to calibrate due to complex multiaxial behavior of ceramic particles under varying stress states. Thus, the following experimental observations are considered to calibrate the parameters of this model:

(i) Under compression, WC has been reported to sustain moderate plastic strain [13,14,49]. The experimental behavior of FGC micropillars under compression is shown in Fig. 13 (a). To fit this experimental data, the parameters of the deviatoric-volumetric boundary of the M7WC model are calibrated to allow sufficient strain-hardening before post-peak softening regime. For this end, only the response of a single simulated typical micropillar has been used. It then yields the optimum values of the parameters c_5, c_6, k_3 and k_4, as shown in Table 3. The WC-WC boundaries oriented at 45° in relation to the compressive load are more susceptible to boundary gliding during micropillar compression [14,49]. Aiming to capture this gliding under compression, the shear boundary parameters k_2 and c_{10} are calibrated to fit this experimental data.

Table 3
Optimum values of the parameters used in microplane model M7WC.

Parameter	Value	Meaning
E	700 *GPa*	Young's modulus
ν	0.24	Poisson's ratio
k_1	$7.3 \bullet 10^{-7}$	Radial scaling parameter
k_2	125	Vertical scaling of shear boundary
c_{10}	$1 \bullet 10^{-2}$	Horizontal scaling of shear boundary
c_5	0.1	Volumetric-deviatoric coupling in the horizontal scaling of the deviatoric boundary
c_6	12	Volumetric-deviatoric coupling in the vertical scaling of the deviatoric boundary
k_3	142.5	Vertical scaling of volumetric boundary
k_4	500	Horizontal scaling of volumetric boundary
c_2	0.28	Tensile yielding in normal boundary

(ii) In WC-Co nanowires under tension, WC particles are shown to undergo little or no plastic deformation [12]. The same happens in WC-Co microbeams under three-point bending [50]. Hence, a large sudden drop on the tensile normal boundary after some elastic deformation is imposed. On the other hand, to determine the tensile strength and fracture energy of FGC, three simulations of notched 3-point bending beam tests of FGC are performed. The specimens and the corresponding load-displacement curves obtained in the simulations are shown in Fig. 5. As expected, this boundary greatly affects crack opening in Mode I. The beams in these simulations are 8550 nm in length, and 1710 nm in width and height. The notch length is 684 nm in all beams. The microstructure of the beams is obtained from the tomography images of the FGC grade. Fracture energy of the FGC is calculated using the work-of-fracture method [51], as given by

$$G_F = \frac{W_F}{b(D - a_0)} \tag{25}$$

where G_F is the fracture energy, W_F is the area under load-displacement curve, b is the width of the beam, D is the height of the beam, and a_0 is the notch length. It is noted that the crack path almost exclusively lies through the WC particles. Thus, using Fig. 5, the fracture energy of WC particles is determined to be 248 ± 34 Jm^{-2}. This range of values is very close to the one reported in [52] as 246 ± 5 Jm^{-2} in Table I for a WC-Co composite with similar microstructural assemblage, in which crack paths remained in WC particles. This step yields the optimum value of the parameter c_2. The optimally calibrated parameters of the M7WC model are shown in Table 3.

3.2. The model MPJ2

Within WC-Co ceramic-metal composites, Co has been reported to have a very high ductility, besides exhibiting a strong interface with WC [13] [53]. In this case, calibration is done by optimally fitting a simple uniaxial tensile test, [10,54,55] as shown in Fig. 6 (a) which allows the determination of the model parameters k_1 and k_2, which control strain-hardening, as well as k_3, which is approximately the yield limit. Elastic modulus and Poisson's ratio are already available from the experiments from [56], but were further optimized to match experimental values used in this section for calibration. The optimal parameters obtained are given in Table 4. The simulated specimen is a dog-bone specimen in which symmetry is considered in two axes as shown in Fig. 6 (b). A mesh of 300 linear hexahedral elements is employed to discretize it.

Damage and fracture have not been included in the formulation of the MPJ2 model because it is found to have negligible influence in the fits of the experimental data used in this study. However, when the elements are distorted too much, i.e. if the absolute value of any of the principal strains exceeds 100% at any one of its Gauss points, they are deleted. Such element deletion introduces some damage and fracture in the material at extremely distorted sites. For this reason, the element size is fixed at approximately 95 nm.

4. Verification

4.1. Nanoindentation of Co binder and WC particles

From now on, the word "prediction" refers to a result from a simulation in which not only the model parameters are kept fixed at their calibrated values but also the element size in the mesh is kept at approximately 95 nm. The nanoindentation predictions on Co binder and WC particles are compared with corresponding experimental data for both materials, obtained from [11] and [10] in Fig. 8 and Fig. 10. In Fig. 7, the indentation is shown on the surface of a 72 μm diameter Co particle at the maximum penetration depth of 1900 nm. It shows the maximum principal logarithmic strain distribution, indicating the possible cracking pattern at the maximum indentation depth after complete unloading of the indenter.

The load-penetration depth prediction, shown in Fig. 8 (a), is used to calculate the hardness-penetration depth response shown in Fig. 8 (b), according to the method described in Ref. [57]. To this end, the initial part of the unloading curve in Fig. 8 (a) is optimally fitted with a straight line ($R^2 = 0.99$), the slope of which is taken as the unloading stiffness. Hardness predicted for the metallic phase is calculated at the maximum penetration depth of 1900 nm as 4.8 ± 0.1 GPa. This value is in total agreement with the one experimentally measured in [10]. The prediction in Fig. 8 (b) nicely approximates the experimental data beyond a shallow depth of about 300 nm. At shallower penetration depths, experimental measurements are known to be unreliable [10]; thus, comparison between prediction and experimental data is not addressed in that very small penetration depths.

Fig. 9 depicts the nanoindentation imprint after unloading on a 36 μm diameter WC particle up to the maximum penetration depth of 900 nm. It shows a very heterogeneous maximum principal strain distribution, indicating the microcrack distribution in the material at the maximum penetration depth after complete unloading of the indenter. This is different from the scenario observed in the indentation imprint on the Co binder (Fig. 7) which shows possible cracking only at the 3 interior edges of the indenter exclusively.

Fig. 10 (a) shows the load-penetration depth prediction resulting from the nanoindentation test. It is in satisfactory agreement with the experimental data obtained for a prismatic plane of WC, except for the tail of the unloading curve. This is also the case for the predicted hardness, as shown in Fig. 9 (b), except at very low penetration depth values. An additional discrepancy is discerned at very high depths,

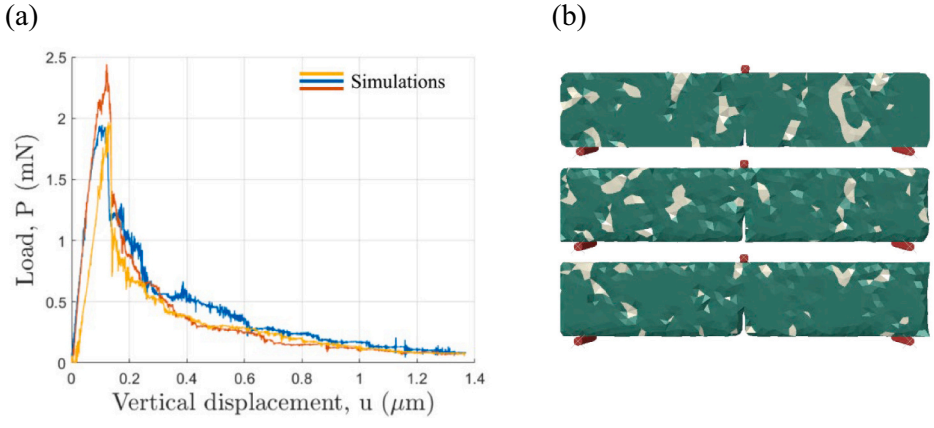

Fig. 5. (a) Three-point bending simulation load-displacement results; (b) geometry and microstructure used in the simulations.

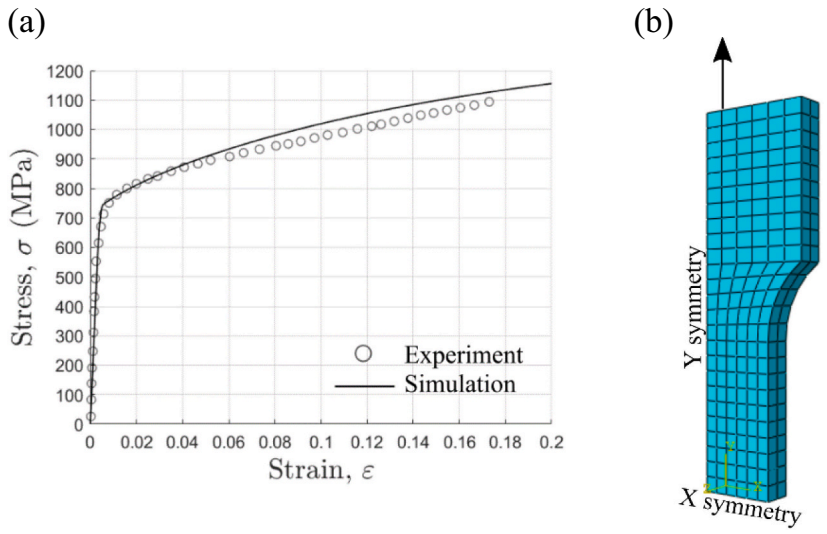

Fig. 6. (a) Uniaxial tension test considered for optimization of J_2-plasticity parameters compared to simulation results; (b) simulated mesh and boundary conditions.

Table 4
Optimum values of the microplane J_2-plasticity model parameters.

Parameter	Value	Meaning
E	230 *GPa*	Young's modulus
ν	0.3	Poisson's ratio
k_1	0.52	Power of hardening law
k_2	0.055	Normalized plastic strain
k_3	620 *MPa*	Approximately the yield strength

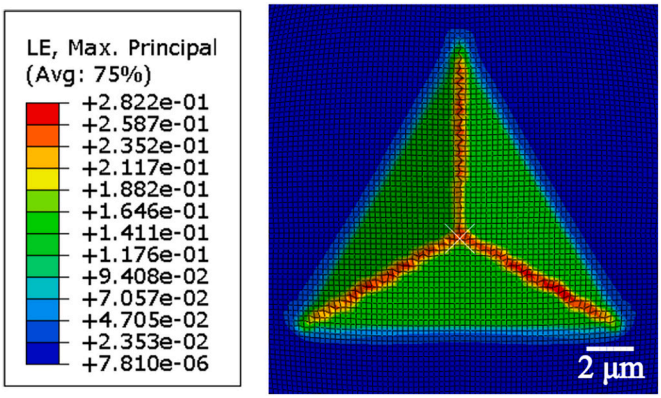

Fig. 7. Final imprint at the end of the prediction of nanoindentation on Co particle.

where hardness values predicted are slightly overestimated. Possible reason for it may be the fact that in the simulation the true microstructure of the material is not used and thus the effect of WC particle being "supported" by the softer Co binder becoming more important as penetration depth increases is missed. The hardness values predicted at maximum penetration depths of 900 and 200 nm are 20.7 ± 0.5 GPa and 20.5 ± 0.5 respectively. The predicted hardness at a maximum penetration depth of 200 nm and the experimental hardness reported for WC prismatic planes at the same maximum penetration depth as 22.0 ± 9.6 GPa [11] agree quite well.

4.2. Nanowires in tension

Useful experimental data on mechanical response of nanowires of WC-Co hardmetals are reported in [12]. Nanowires used in these experiments had WC particles with an average size of 2 μm, similar to the CGCs. They are classified as non-segmentalized or segmentalized, depending on if they exhibit a continuous structure of WC throughout its length or not. Nanowires are also classified according to the area fraction of Co observed on their top and side surfaces. In general, all specimens having a Co area fraction above 20% are segmentalized, while those with metallic area fraction under 20% may be segmentalized or non-segmentalized.

Nanowire specimens used in the predictions, shown in Fig. 11 (a), have a mean area fraction of 12.7 ± 5.4% and are all non-segmentalized. Accordingly, the predictions are to be compared with the test results from the non-segmentalized nanowires reported in [12]. All nanowires are structured with CGC S-FIB tomography, as this grade is constituted by carbides whose mean size is similar to the one reported in the experimental study. As the modelled nanowires do not have the exact same microstructure as those tested in [12], and the simulated microstructures are chosen randomly, some deviation in the predictions from the experimental values is to be expected. Consequently, Fig. 11 (b) depicts a slight deviation in the prediction. However, it is noted that the prediction curve is still well within the 95% confidence intervals. The predicted mean tensile strength turns out to be 4.30 ± 1.40 GPa which is close to the experimentally reported range of values given as. 4.69 ± 0.60 GPa in [15].

In all predictions seen in Fig. 12, a linear-elastic initial part of the stress-strain curve is followed by a sharp drop in the stress, caused by the brittle fracturing of the WC particles. This figure is primarily useful to create the predicted strength range for the nanowires.

4.3. Micropillars in compression

Predictions from twelve simulations on FGC and CGC micropillar specimens are compared with experimental data given in [13,14], as shown in Fig. 13. In Fig. 13 (a), stress-strain curves are calculated from the measured load-displacement data considering a cross-sectional area 1 μm below the top of the micropillars [14]. Meanwhile, in Fig. 13 (b) such curves are calculated considering a cross-sectional area at three-fourths of the total length of the micropillar. The indenters are assumed to be inclined by 1.25° and 2.10° relative to the top surface of the micropillars for the CGC and FGC micropillars respectively to be able to fit the initial part of the stress-strain curves observed in experiments (see Fig. 15 for comparison). These inclination angles mean imperfect contact conditions between indenter and micropillar. Since the micropillars are randomly obtained from real tomography images, there is

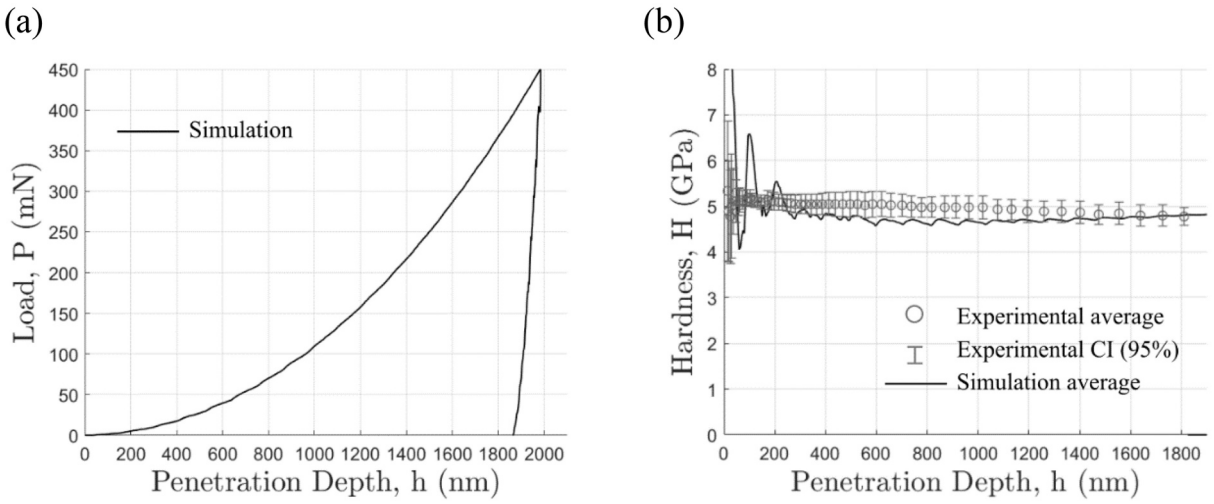

Fig. 8. Nanoindentation testing of metallic phase: (a) predicted load-penetration depth curve; and (b) comparison of hardness-penetration depth prediction curve with corresponding experimental data from [10].

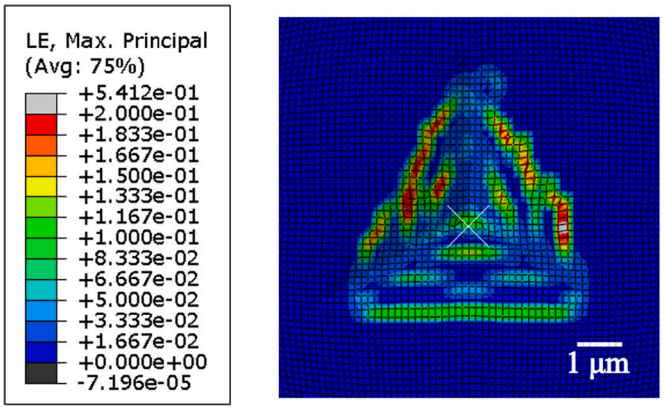

Fig. 9. Final imprint at the end of the prediction of nanoindentation on WC particle.

variation in the stress-strain response obtained in the simulations as shown in Fig. 13 (a) and Fig. 13 (b).

In Fig. 14, the mean values of experimental data and predictions, both with a 95% confidence interval, are shown for FGC and CGC micropillars. The prediction curves are well within the experimental confidence intervals for both types of composites. The confidence interval of the FGC predictions is much narrower than that of the CGC case, as seen in Fig. 14 (a). This indicates that micropillars of FGC are closer to the representative volume element (RVE) of the microstructure than in the case of CGC ones. Nevertheless, the relatively good fit in Fig. 14 (b) points out that the six predictions considered are also representative of the corresponding microstructure.

In the simulations shown in Fig. 15, a perfect contact is assumed between the indenter and the top surface of the micropillar. In this case, a linear elastic response is observed in in the initial part of the simulated stress-strain curves. However, it does not capture experimental observations of a non-linear initial part. Moreover, the overall stress-strain response prediction for the FGC micropillars grossly overshoots experimental values. Thus, from Fig. 14 and Fig. 15 it may concluded that the experiments involved a misalignment at the contact surface between indenter and micropillar of about 1.25° and 2.10° for CGC and FGC specimens respectively.

Table 5 compares the experimental and predicted unloading stiffness of FGC and CGC specimens. It can be inferred from this table that the imperfect contact conditions do not persist at high compressive loads.

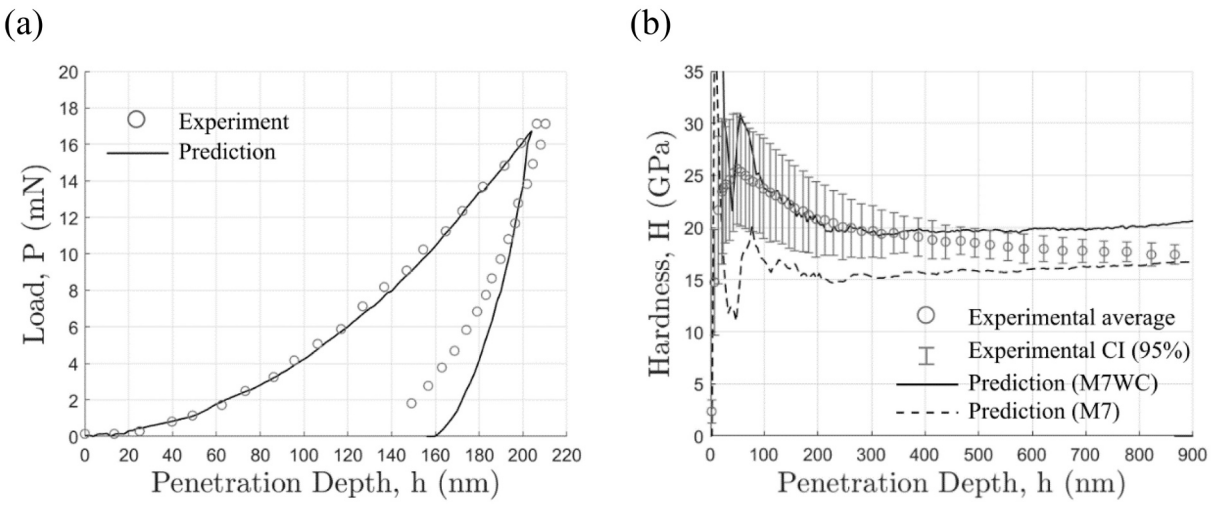

Fig. 10. Nanoindentation testing of WC carbides (a) prediction load-penetration depth compared to the experimental curve; (b) comparison of the predicted hardness-penetration depth curve with M7WC, M7 models and corresponding experimental data from [11].

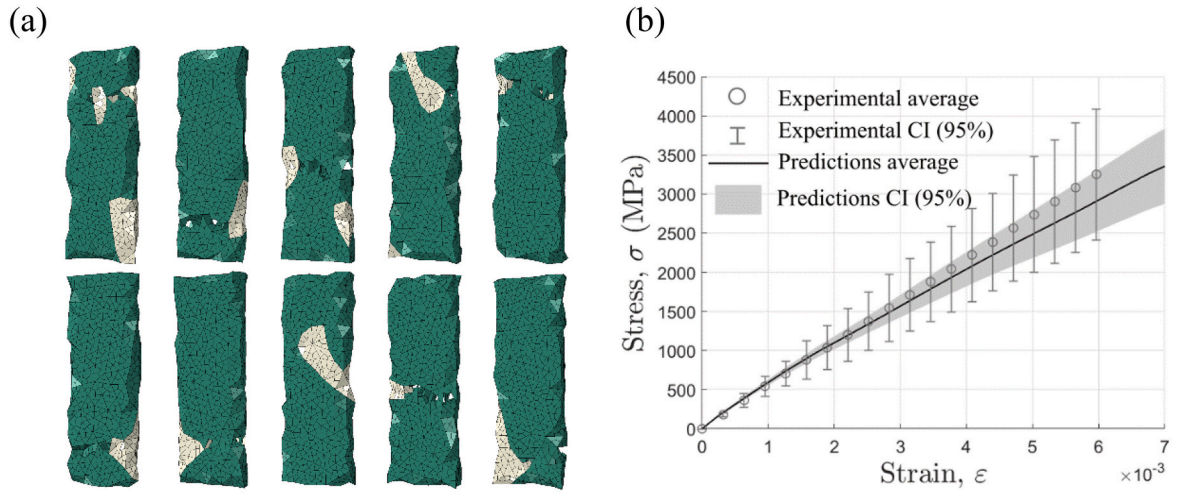

Fig. 11. (a) Nanowire meshes used in the predictions; and (b) comparison of predicted uniaxial tensile test response of nanowires and the corresponding experimental data from [12].

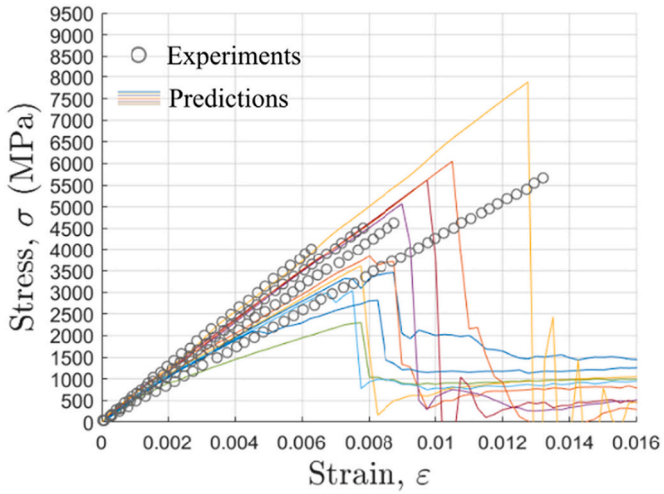

Fig. 12. Predictions plotted separately against experimental data from [12] to determine the predicted strengths.

Simulation scenarios of compressed micropillars are shown in Fig. 16. Equivalent deviatoric stresses for Co binder and maximum principal strains for WC particles for FGC composite are shown in Fig. 16 (a). Equivalent plastic stresses seem to be moderate in the binder phase, but maximum principal strains are observed to be in the finite strain regime. Regarding the ceramic phase, the plotted maximum principal strains point out cracking paths: fissures inclined at 45° and vertical cracks parallel to the compression load, which are archetypical features of cracking in quasi-brittle materials. Predicted outcomes for CGC are given in Fig. 16 (b) where it is observed that equivalent deviatoric stresses are concentrated at or near the WC-Co interfaces, together with cracks in the WC particles, mostly appearing at WC-WC grain boundaries. This cracking scenario is similar to the one discerned after experimental tests, as shown in Fig. 16.

In the case of FGC micropillars, because of the relatively low binder content, irreversible deformation phenomena is linked to (mainly) WC-WC boundary gliding and dislocation movement within individual carbides, as shown in Fig. 17 by arrows marked as (1) and (3) respectively. On the other hand, because of the higher binder content within CGC specimens, plastic strain in this case occurs within the metallic phase, as shown in Fig. 17 by arrows marked as (2). According to [14], both WC-WC boundaries cracks and WC-Co interface cracks were observed in

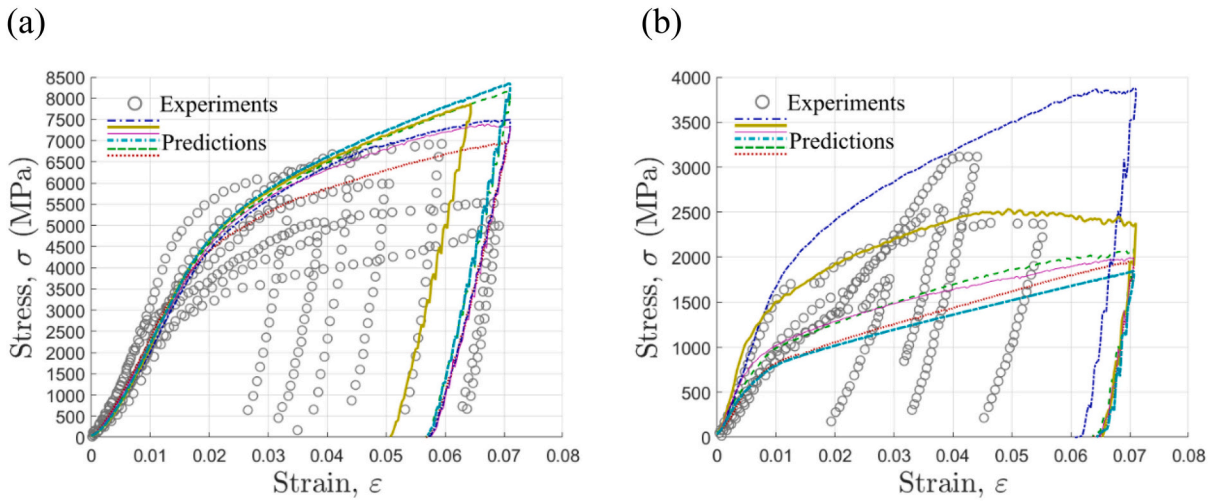

Fig. 13. Predicted stress-strain curves from micropillar simulations plotted against experimental data of (a) FGC tested in Sandoval et al. [14]; and (b) CGC tested in Tarragó et al. [13].

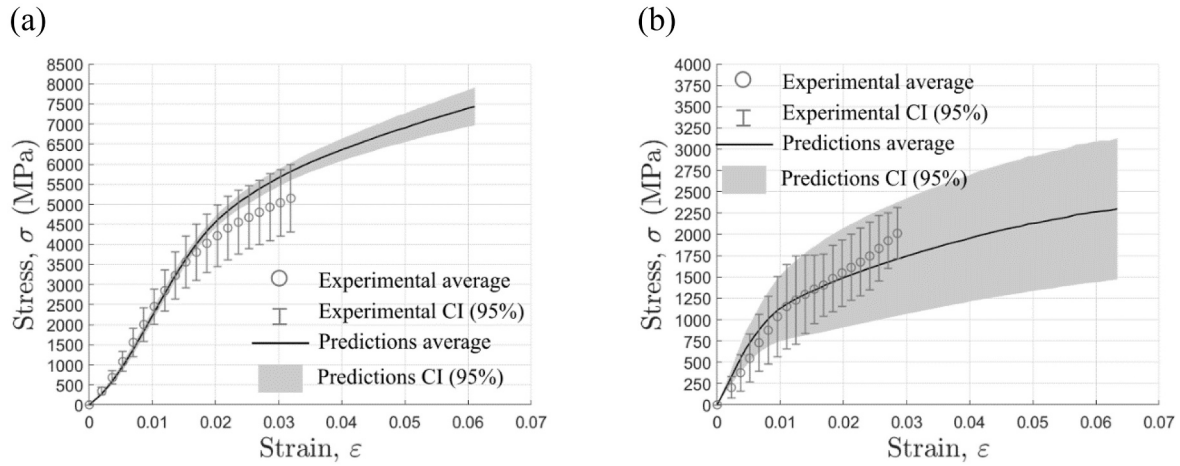

Fig. 14. Average and confidence intervals of predicted and experimental stress-strain curves using imperfect contact for (a) FGC and (b) CGC micropillars.

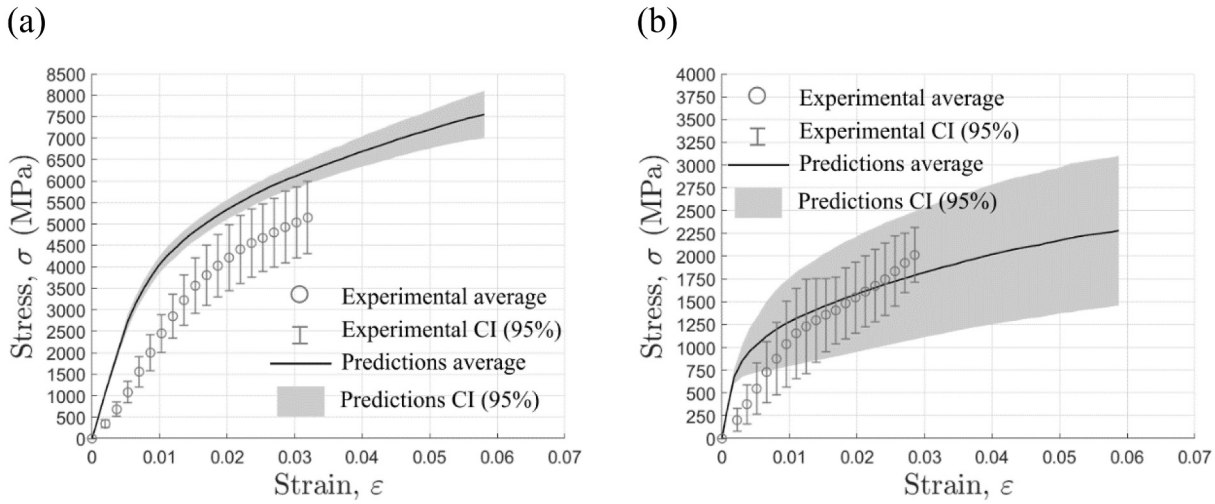

Fig. 15. The predicted stress-strain curves using perfect contact for (a) FGC and (b) CGC micropillars.

Table 5
Comparison of predicted and experimental stiffness values, from unloading testing stage.

	FGC	CGC
Experimental unloading stiffness (GPa)	625 ± 103	270 ± 31
Predicted unloading stiffness, assuming perfect contact (GPa)	639 ± 24	347 ± 78
Predicted unloading stiffness, assuming imperfect contact (GPa)	623 ± 52	334 ± 59

several specimens of micropillars under compression. However, cracks in WC-WC boundaries were much more prevalent independently of the grade analyzed. This is an indication that such regions are favorable the initiation and extension of cracks, as depicted in Fig. 17. According to [14], both WC-WC boundaries cracks and WC-Co interface cracks were observed in several specimens of micropillars under compression. However, cracks in WC-WC boundaries were much more prevalent independently of the grade analyzed. This is an indication that such regions are favorable the initiation and extension of cracks, as depicted in Fig. 17. At WC-Co interfaces the well-known stress concentration at a bimaterial interface [58,59] in which the materials stiffnesses are very different are observed, so it is automatically captured by the proposed computational framework.

Regarding WC-WC grain boundaries, inclined microplanes experiencing higher resolved shear stress reached their strengths earlier and experienced cracking. As a consequence, extension of cracking strains at the macrolevel are obtained at an inclined angle, as shown in Fig. 16 and Fig. 18. Moreover, and as expected, the predictions highlights the key role played by sharp corners and grooves in the carbides as crack nucleation sites, many of which are WC-WC boundaries, as shown in Fig. 18. It is also very interesting that no special numerical treatment is used in the simulations to capture cracking at these boundaries.

After reaching the elastic limit, WC particles may sustain moderate plastic strain [49,60,61,62]. In the predictions of micropillar compressive behavior, both the deviatoric and shear boundaries are active. Hence, the strain-hardening observed in Fig. 13 and Fig. 14 can be controlled by adjusting the parameters of these two stress-strain boundaries. Microplanes experiencing increasing deviatoric compressive strain will eventually reach post-peak softening regime causing inclined cracks and cracks in the direction of loading.

As WC-Co interfaces are known to be critical regions for crack propagation [19,53], in the predictions the Co binder is observed to undergo large strains as the carbides move and rotate during loading, as shown in Fig. 19. As a consequence of this significant relative movement between carbides, severe strains in the Co binder are induced, resulting in toughening of the composite by means of ductile-ligament bridging [8,53]. This is indeed the primary strengthening role of the metallic

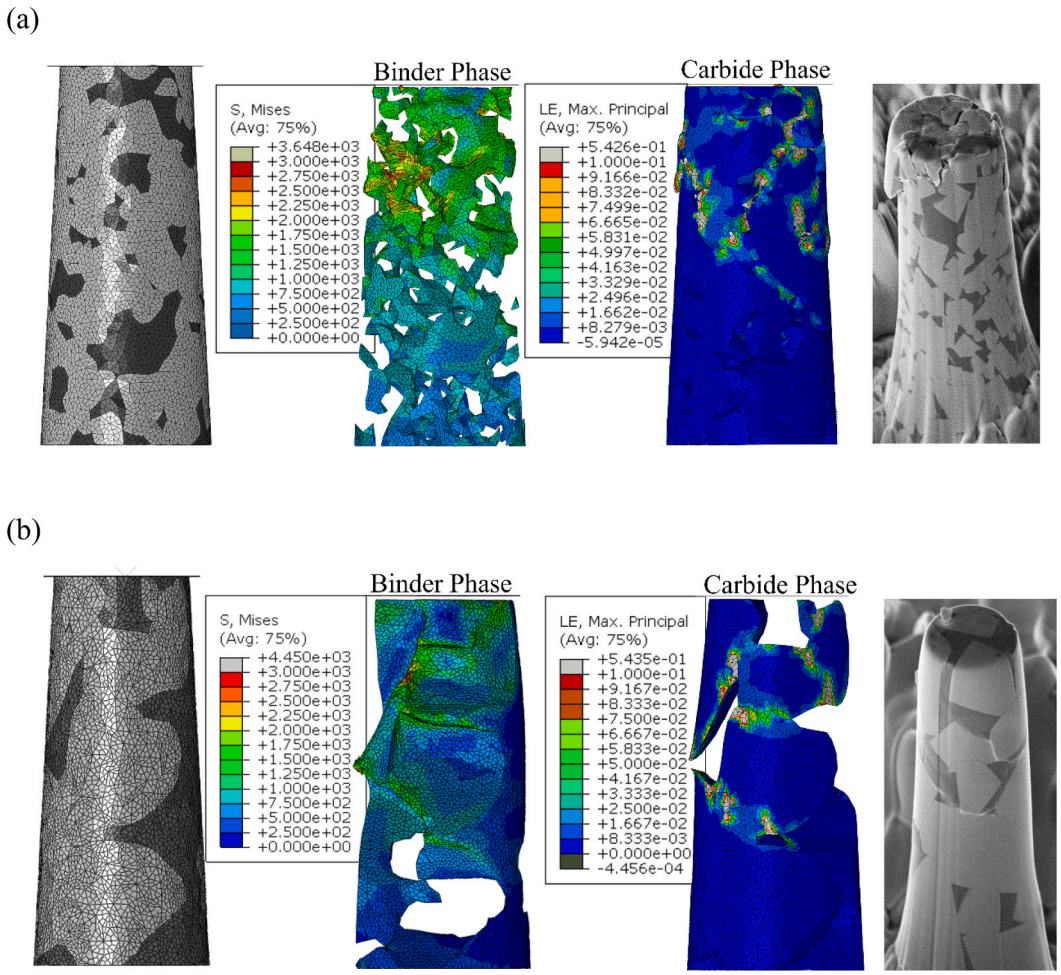

Fig. 16. Micropillar compression of (a) FGC and (b) CGC specimens: predicted deformation/cracking scenario and experimental observations [14]. Stresses are in MPa.

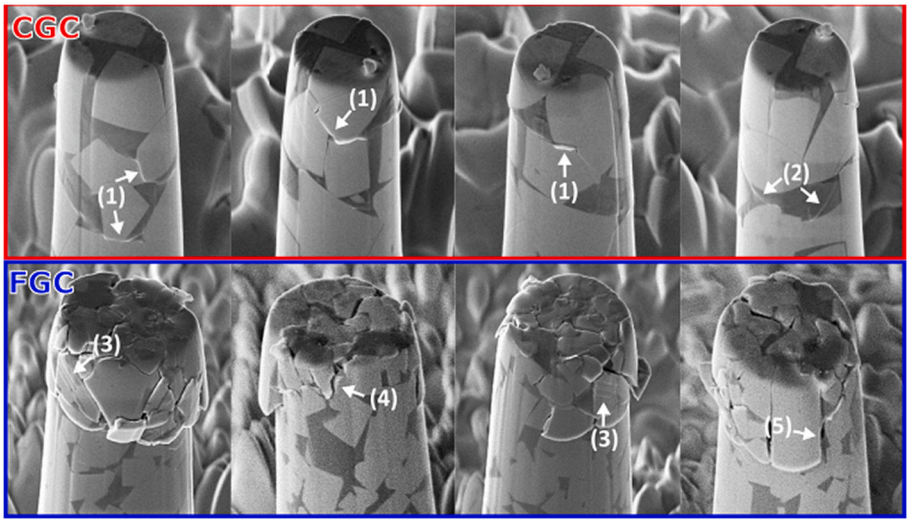

Fig. 17. Experimental observations: WC-WC boundary glide (1); plastic deformation within binder (2); slip planes activation in WC particles (3); 45° cracks (4); crack at Co/WC boundary (5). Reproduced with the permission from [14].

binder in cemented carbides [4,5,6,7,9], and such experimental fact is also satisfactorily captured by the simulation. This is clearly illustrated in Fig. 20 (a) and Fig. 20 (b) where it may be discerned that cracks are effectively arrested when they reach the Co binder, in agreement with the experimental observations [52,53].

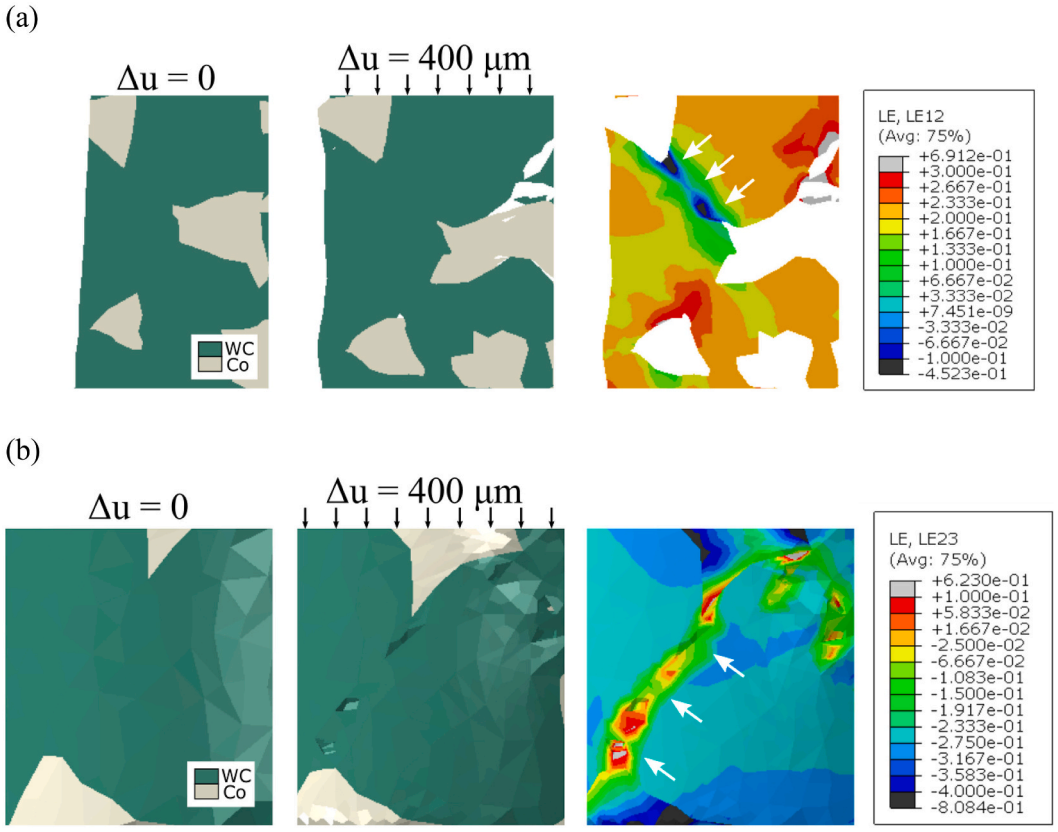

Fig. 18. Strain concentration in sharp grooves and corners of the mesh, typically found at WC-WC boundaries for (a) FGC and (b) CGC micropillars.

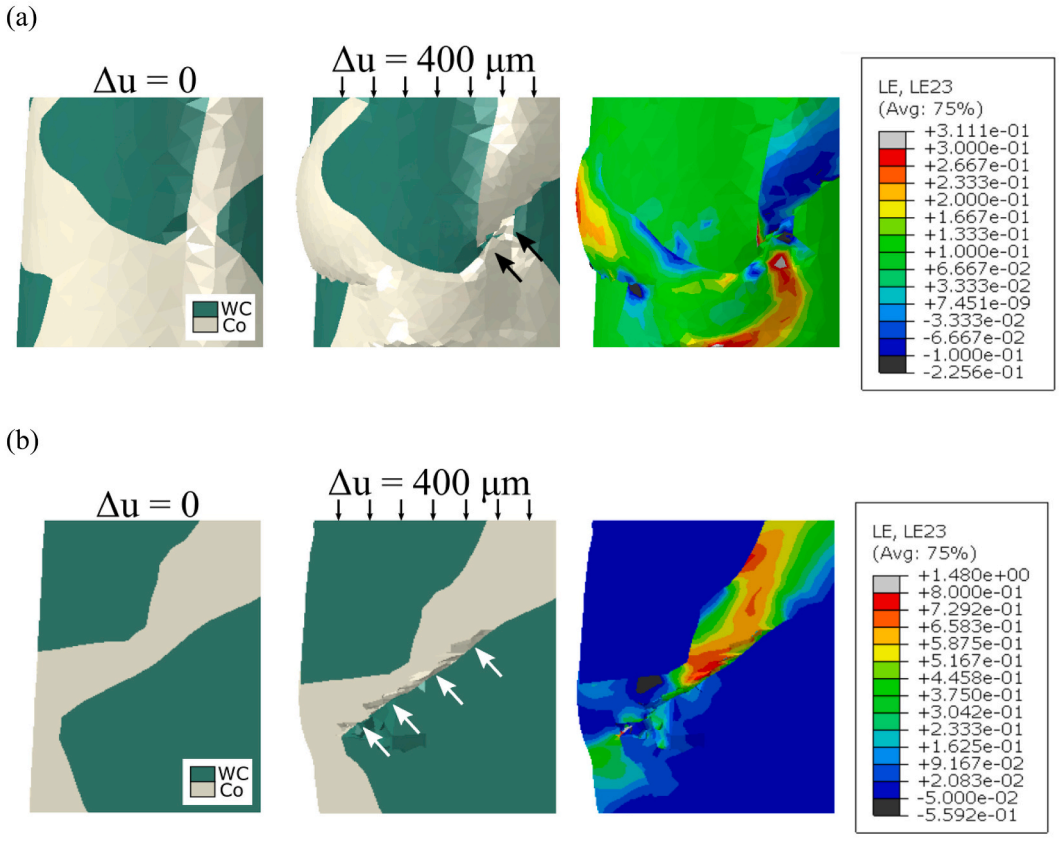

Fig. 19. Shear strain in the binder between two rotating WC particles in (a) and (b).

5. Conclusions

In this study, a microplane-based computational framework is developed for the finite element analysis of WC-Co hard metals. The finite element meshes are obtained from FIB tomography images of the *real* WC-Co composites, removing any possibility of spurious geometric features likely to happen in the case of computationally generated meshes, which can influence stress concentration and consequently crack initiation and propagation. Then, two distinct microplane constitutive models are developed for each phase in the simulations: model MPJ2 for the Co binder and the microplane model M7WC for the WC particles. The optimization of the model MPJ2 parameters is carried out considering uniaxial tension data, while the parameters of the model M7WC are optimized considering a single simulation of a micropillar under compression on the FGC and the experimental fracture energy of FGC in Mode I via 3-point bending simulations. Finally, the methodology was verified against (1) nanoindentation experiments of both WC and Co phases, (2) nanowire tension experiments and (3) micropillar compression experiments. The prediction curves are shown to match very well the experimental data with few exceptions. The following conclusions are drawn from this study:

(i) The proposed computational framework could predict: the hardness of both WC carbides and the Co binder in nanoindentation; the tensile response and tensile strength of non-segmentalized nanowires; and compressive response of several micropillars of two different grades (without considering the single micropillar simulation used for model calibration).

(ii) It is found out that the indenter in the experiments has an inclination relative to the top surface of the micropillars at 1.25° and 2.10° for the CGC and FGC respectively. Thus, the imperfect contact between indenter and micropillar greatly effects the initial mechanical response. On the other hand, the stiffness calculated with the unloading part of the stress-strain curves from simulations agree well with the reported experimental values and these values are insensitive to the indenter inclination.

(iii) The simulation of indentation at shallow depths is challenging in both WC particles and Co binder. Further mesh refinement is known to help only marginally. However, experimental data is also known to be not representative of the material response at such shallow penetration depths due to difficult-to-control surface effects. It is found that for sufficiently accurate indentation simulations, the diameter of the discretized half space should be at least 36 times larger than the max. Penetration depth for both WC and Co phases. Larger diameters may increase the computational cost but little to no improvements may be achieved in the predictions.

(iv) According to nanoindentation predictions there is distributed microcracking in the WC particles. In micropillar compression simulations, sharp geometric features such as those found in the WC-WC interfaces were main source of cracks, which propagated at inclined angles as experimental observations show. In non-segmentalized nanowires under tension, the stress-strain response shows little or no plastic deformation, agreeing well with experiments done in WC-Co hardmetal under tension. Under compression, WC is known to be able to sustain moderate plastic strain, while in tension it has a very brittle behavior. Model M7WC can discern both cases due to the built-in normal, volumetric, shear and deviatoric boundaries which govern both the tensile and compressive behaviors of the WC particle.

(v) The Co binder region neighboring the WC carbides is found to undergo high strains as carbides rotate and move during the micropillar compression. This is likely the cause of crack initiation in these zones, as observed in the experiments. The

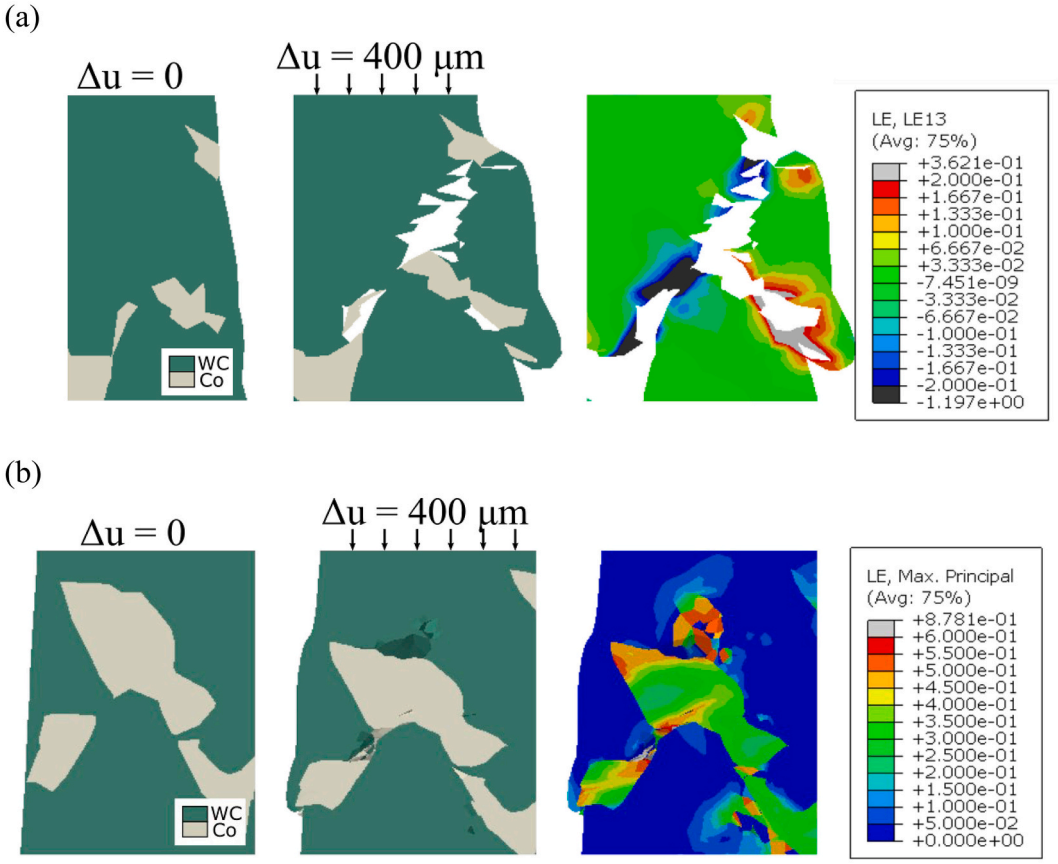

Fig. 20. (a) Cracked carbides bridged by ductile ligaments of the metallic phase; (b) crack arrest when it impinges the Co binder.

mechanism of "Co-binder bridging" widely known in literature is captured in the predictions of micropillar simulations. Such high plastic strains are found to toughen the composite and arrest the cracks passing through the WC particles. The use of the work conjugate Kirchoff stress and logarithmic strain tensors in the MPJ2 model makes it possible to reproduce these large strain mechanisms.

The use of the microplane approach for both WC and Co phases along with the real microstructure predicts the deformation and fracture of all experiments analyzed. This approach can be applied to other loading configurations, such as cyclic loads, to WC-Co composites with varying ratios of WC particles, and even to other cermets.

CRediT authorship contribution statement

Pedro Vinícius Sousa Machado: Conceptualization, Data curation, Formal analysis, Investigation, Methodology, Software, Validation, Visualization, Writing – original draft. **Ferhun C. Caner:** Conceptualization, Formal analysis, Investigation, Methodology, Software, Supervision, Validation, Writing – review & editing. **Luis Llanes:** Funding acquisition, Project administration, Resources, Writing – review & editing. **Emilio Jimenez Pique:** Conceptualization, Funding acquisition, Investigation, Project administration, Resources, Supervision, Writing – review & editing.

Declaration of Competing Interest

The Authors declare no Competing Financial or Non-Financial Interests.

Data availability

The datasets generated during and/or analyzed during the current study are not publicly available due to confidentiality agreement with the funding company but are available from the corresponding author on reasonable request.

Acknowledgements

The study was supported by the Spanish Ministerio de Ciencia, Innovación y Universidades MICINN - FEDER (Spain) through grant numbers PGC2018-096855-B-C41 and PID2019-106631GB-C41. The first author would like to acknowledge the scholarship provided by CIEFMA research group and UPC through the grant no. FIB-UPC 2020.

References

[1] L. Prakash, Comprehensive Hard Materials, Elsevier, 2014, pp. 29–90.
[2] H.E. Exner, Physical and chemical nature of cemented carbides, Int. Metals Rev. 24 (1) (1979) 149–173.
[3] J. Gurland, New scientific approaches to development of tool materials, Int. Mater. Rev. 33 (1988) 151–166.
[4] L.S. Sigl, P.A. Mataga, B.J. Dalgleish, R.M. McMeeking, A.G. Evans, On the toughness of brittle materials reinforced with a ductile phase, Acta Metall. 36 (4) (1988) 945–953.
[5] L.S. Sigl, H.E. Exner, The flow stress and hardness of metal-reinforced brittle composites, Mater. Sci. Eng. A 108 (1989) 121–129.
[6] L.S. Sigl, H.F. Fischmeister, On the fracture toughness of cemented carbides, Acta Metall. 36 (4) (1988) 887–897.
[7] J. Tarragó, E. Jiménez-Piqué, L. Schneider, D. Casellas, Y.T.A.L. Llanes, FIB/FESEM experimental and analytical assessment of R-curve behavior of WC–Co cemented carbides, Mater. Sci. Eng. A 645 (2015) 142–149.
[8] J. Tarragó, D. Coureaux, Y. Torres, D. Casellas, I. Al-Dawery, L. Schneider, L. Llanes, Microstructural effects on the R-curve behavior of WC-Co cemented carbides, Mater. Des. 97 (2016) 492–501.
[9] J.M. Tarragó, D. Coureaux, Y. Torres, E. Jiménez-Piqué, L. Schneider, J. Fair, L. Llanes, Strength and reliability of WC-Co cemented carbides: understanding microstructural effects on the basis of R-curve behavior and fractography, Int. J. Refract. Met. Hard Mater. 71 (2018) 221–226.
[10] J.J. Roa, E. Jiménez-Piqué, J.M. Tarragó, M. Zivcec, C. Broeckmann, L. Llanes, Berkovich nanoindentation and deformation mechanisms in a hardmetal binder-like cobalt alloy, Mater. Sci. Eng. A 621 (2015) 128–132.
[11] J.J. Roa, E. Jimenez-Pique, C. Verge, J.M. Tarragó, A. Mateo, J. Fair, L. Llanes, Intrinsic hardness of constitutive phases in WC-Co composites: nanoindentation testing, statistical analysis, WC crystal orientation effects and flow stress for the constrained metallic binder, J. Eur. Ceram. Soc. 35 (13) (2015) 3419–3425.
[12] T.M. Takahiro Namazu, H. Akamine, T. Fujii, K. Kuroda, Y. Takami, Mechanical reliability of FIB-fabricated WC-Co cemented carbide nanowires evaluated by MEMS tensile testing, Eng. Fract. Mech. 150 (2015) 126–134.
[13] J.M. Tarragó, J.J. Roa, E. Jiménez-Piqué, E. Keown, J. Fair, L. Llanes, Mechanical deformation of WC-Co composite micropillars under uniaxial compression, Int. J. Refract. Met. Hard Mater. 54 (2016) 70–74.
[14] D.A. Sandoval, A. Rinaldi, A. Notargiacomo, O. Ther, E. Tarrés, J.J. Roa, Influence of specimen size and microstructure on uniaxial compression of WC-Co micropillars, Ceram. Int. 45 (13) (2019) 15934–15,941.
[15] H. Zhang, B.E. Schuster, Q. Wei, K.T. Ramesh, The design of accurate micro-compression experiments, Scr. Mater. 54 (2) (2006) 181–186.
[16] D. Kiener, C. Motz, M. Rester, M. Jenko, G. Dehm, FIB damage of Cu and possible consequences for miniaturized mechanical tests, Mater. Sci. Eng. A 459 (1) (2007) 262–272.
[17] D. Kiener, C. Motz, G. Dehm, Micro-compression testing: a critical discussion of experimental constraints, Mater. Sci. Eng. A 505 (1) (2009) 79–87.
[18] G. Dehm, B.N. Jaya, R. Raghavan, C. Kirchlechner, Overview on micro- and nanomechanical testing: new insights in interface plasticity and fracture at small length scales, Acta Mater. 142 (2018) 248–282.
[19] H.F. Fischmeister, S. Schamauder, L.S. Sigl, Finite element modelling of crack propagation in WC-Co hard metals, Mater. Sci. Eng. A 105–106 (1988) 305–311.
[20] T. Sadowski, T. Nowicki, Numerical investigation of local mechanical properties of WC/Co composite, Comput. Mater. Sci. 43 (1) (2008) 235–241.
[21] U.A. Ozden, A. Bezold, C. Broeckmann, Numerical simulation of fatigue crack propagation in WC / Co based on a continuum damage mechanics approach, Procedia Mater. Sci. 3 (2014) 1518–1523.
[22] W. Kayser, A. Bezold, C. Broeckmann, Simulation of residual stresses in cemented carbides, Int. J. Refract. Met. Hard Mater. 63 (2017) 55–62.
[23] D. Hubert, S. Tomasz, Modelling of the damage process of interfaces inside the WC/Co composite microstructure: 2-D versus 3-D modelling technique, Compos. Struct. 159 (2017) 121–127.
[24] D. Tkalich, G. Cailletaud, V.A. Yastrebov, A. Kane, A micromechanical constitutive modeling of WC hardmetals using finite-element and uniform field models, Mech. Mater. 105 (2017) 166–187.
[25] U.A. Ozden, G. Chen, A. Bezold, C. Broeckmann, Numerical investigation on the size effect of a WC/Co 3D representative volume element based on the homogenized elasto-plastic response and fracture energy dissipation, Key Eng. Mater. 592–593 (2013) 153–156.
[26] E. Jiménez-Piqué, M. Turon-Vinas, H. Chen, T. Trifonov, J. Fair, E. Tarrés, L. Llanes, Focused ion beam tomography of WC-Co cemented carbides, Int. J. Refract. Met. Hard Mater. 67 (2017) 9–17.
[27] U.A. Özden, K. Jiang, A. Bezold, C. Broeckmann, Evaluation of fatigue crack growth performance in different hardmetal grades based on finite element simulation, Proc. Struct. Integr. 2 (2016) 648–655.
[28] D. Tkalich, G. Cailletaud, V. Yastrebov, A. Kane, Multiscale modeling of cemented tungsten carbide in hard rock drilling, Int. J. Solids Struct. 128 (2017) 282–295.
[29] W. Kayser, S. van Kempen, A. Bezold, M. Boin, R. Wimpory, C. Broeckmann, Numerical investigation the of WC re-precipitation impact on the residual stress state in WC20 wt.-%Co hardmetal, Int. J. Refract. Met. Hard Mater. 84 (2019).
[30] U.A. Özden, K.P. Mingard, M. Zivcec, A. Bezold, C. Broeckmann, Mesoscopical finite element simulation of fatigue crack propagation in WC/Co-hardmetal, Int. J. Refract. Met. Hard Mater. 49 (1) (2015) 261–267.
[31] S. Herd, R.J. Wood, J.A. Wharton, C.F. Higgs, Explicit fracture modelling of cemented tungsten carbide (WC-Co) at the mesoscale, Mater. Sci. Eng. A 712 (2018) 521–530.
[32] G. Chen, U.A. Ozden, A. Bezold, C. Broeckmann, A statistics based numerical investigation on the prediction of elasto-plastic behavior of WC-Co hard metal, Comput. Mater. Sci. 80 (2013) 96–103.
[33] L. Faksa, W. Daves, T. Klünsner, K. Maier, T. Antretter, C. Czettl, W. Ecker, Shot peening-induced plastic deformation of individual phases within a coated WC-Co hard metal composite material including stress-strain curves for WC as a function of temperature, Surf. Coat. Technol. 380 (2019).
[34] K. Jiang, A. Bezold, C. Broeckmann, Numerical modeling of the progressive damage in the microstructure of WC-Co hardmetals under fatigue loading, Proc. Struct. Integr. 23 (2019) 451–456.
[35] W. Kayser, A. Bezold, C. Broeckmann, EBSD-based FEM simulation of residual stresses in a WC6wt.-%Co hardmetal, Int. J. Refract. Met. Hard Mater. 73 (2018) 139–145.
[36] H. Debski, T. Sadowski, Modelling of the damage process of interfaces inside the WC/Co composite microstructure: 2-D versus 3-D modelling technique, Compos. Struct. 159 (2017) 121–127.
[37] M. Brocca, Z.P. Bazant, Microplane constitutive model and metal plasticity, Appl. Mech. Rev. 53 (10) (2000) 265–281.
[38] F.C. Caner, Z.P. Bazant, Microplane Model M7 for plain concrete. I: formulation, J. Eng. Mech. 139 (12) (2013) 1714–1723.
[39] F.C. Caner, Z.P. Bazant, Microplane Model M7 for plain concrete. II: calibration and verification, J. Eng. Mech. 139 (12) (2013) 1724–1735.

[40] Z.P. Bazant, J. Planas, Crack band models and smeared cracks, in: Fracture and Size Effect in Concrete and Other Quasibrittle Materials, Routledge, Boca Raton, 1998, pp. 213–259.
[41] F.C. Caner, Z.P. Bazant, R. Wendner, Microplane model M7f for fiber reinforced concrete, Eng. Fract. Mech. 105 (2013) 41–57.
[42] K. Kirane, Z.P. Bazant, Microplane damage model for fatigue of quasibrittle materials: Subcritical crack growth, lifetime and residula strength, Int. J. Fatigue 70 (2015) 93–105.
[43] S. Rahimi-Aghdam, Z.P. Bažant, F.C. Caner, Diffusion-Controlled and creep-mitigated ASR damage via microplane model, J. Eng. Mech. 143 (2) (2017).
[44] Z.P. Bazant, F.C. Caner, Impact comminution of solids due to local kinetic energy of high shear strain rate: I Continuum theory and turbulence analogy, J. Mech. Phys. Solids 64 (2014) 223–235.
[45] Z.P. Bazant, P.G. Gambarova, Crack shear in concrete: crack band microplane model, J. Struct. Eng. 110 (9) (1984) 2015–2035.
[46] F.C. Caner, Z.P. Bazant, J. Cervenka, Vertex effect in strain-softening concrete at rotating principal axes, J. Eng. Mech. 128 (1) (2002) 24–33.
[47] L.E. Malvern, Introduction to the Mechanics of Continuous Medium, Prentice-Halls, 1969.
[48] C. Jacobi, Über ein leichtes Verfahren die in der Theorie der Säcularstörungen vorkommenden Gleichungen numerisch aufzulösen, J. Reine Angew. Math. 1846 (30) (1846) 51–94.
[49] T. Csanádi, M. Bl'anda, A. Duszová, N.Q. Chinh, P. Szommer, J. Dusza, Deformation characteristics of WC micropillars, J. Eur. Ceram. Soc. 34 (15) (2014) 4099–4103.
[50] M. Elizalde, J.A.I. Ocaña, J. Sánchez-Moreno, Mechanical strength assessment of single WC-WC interfaces present in WC-Co hardmetals through micro-beam bending experiments, Int. J. Refract. Met. Hard Mater. 72 (2018) 39–44.
[51] Z.P. Bazant, J. Planas, Experimental determination of cohesive crack properties, in: Fracture and Size Effect in Concrete and Other Quasibrittle Materials, Routledge, Boca Raton, 1998, pp. 180–190.
[52] L.S. Sigl, H.E. Exner, Experimental study of the mechanics of fracture in WC-Co alloys, Metall. Trans. A. 18 (7) (1987) 1299–1308.
[53] J.M. Tarragó, E. Jiménez-Piqué, M. Turon-Vinas, L. Rivero, I. Al-Dawery, L. Schneider, L. Llanes, Fracture and fatigue behavior of cemented carbides: 3D focused ion beam tomography of crack-microstructure interactions, Int. J. Powder Metallur. 50 (4) (2014) 33–42.
[54] B. Roebuck, E. Almond, A. Cottenden, The influence of composition, phase transformation and varying the relative F.C.C. and H.C.P. phase contents on the properties of dilute CoWC alloys, Mater. Sci. Eng. 66 (2) (1984) 179–194.
[55] B. Roebuck, E.A. Almond, Deformation and fracture processes and the physical metallurgy of WC–Co hardmetals, Int. Mater. Rev. 33 (1) (1988) 90–112.
[56] U.A. Özden, K.P. Mingard, M. Zivcec, A. Bezold, C. Broeckmann, Mesoscopical finite element simulation of fatigue crack propagation in WC/Co-hardmetal, Int. J. Refract. Met. Hard Mater. 49 (2015) 261–267.
[57] W.C. Oliver, G.M. Pharr, An improved technique for determining hardness and elastic modulus using load displacement sensing indentation experiments, J. Mater. Res. 7 (6) (1992) 1564–1583.
[58] N. Somaratna, T.C.T. Ting, Three-dimensional stress singularities in anisotropic materials and composites, Int. J. Eng. Sci. 24 (7) (1986) 1115–1134.
[59] C.S. Huanga, A.W. Leissab, Stress singularities in bimaterial bodies of revolution, Compos. Struct. 82 (4) (2008) 488–498.
[60] V. Sarin, T. Johannesson, On the deformation of WC–Co cemented carbides, Metal Sci. 9 (1) (1975) 472–476.
[61] R. Warren, Measurement of the fracture properties of brittle solids by hertzian indentation, Acta Metall. 26 (11) (1978) 1759–1769.
[62] H. Zhang, Z. Fang, Characterization of quasi-plastic deformation of WC–Co composite using Hertzian indentation technique, Int. J. Refract. Met. Hard Mater. 26 (2008) 106–114.